MIRT: A Simultaneous Reconstruction and Affine Motion Compensation Technique for Four Dimensional Computed Tomography (4DCT)[*]

Anh-Tuan Nguyen[†], Jens Renders[†], Domenico Iuso[†], Yves Maris[†], Jeroen Soete[‡], Martine Wevers[‡], Jan Sijbers[†], and Jan De Beenhouwer[†]

Abstract. In four-dimensional computed tomography (4DCT), 3D images of moving or deforming samples are reconstructed from a set of 2D projection images. Recent techniques for iterative motion-compensated reconstruction either necessitate a reference acquisition or alternate image reconstruction and motion estimation steps. In these methods, the motion estimation step involves the estimation of either complete deformation vector fields (DVFs) or a limited set of parameters corresponding to the affine motion, including rigid motion or scaling. The majority of these approaches rely on nested iterations, incurring significant computational expenses. Notably, despite the direct benefits of an analytical formulation and a substantial reduction in computational complexity, there has been no exploration into parameterizing DVFs for general affine motion in CT imaging. In this work, we propose the Motion-compensated Iterative Reconstruction Technique (MIRT)- an efficient iterative reconstruction scheme that combines image reconstruction and affine motion estimation in a single update step, based on the analytical gradients of the motion towards both the reconstruction and the affine motion parameters. When most of the state-of-the-art 4DCT methods have not attempted to be tested on real data, results from simulation and real experiments show that our method outperforms the state-of-the-art CT reconstruction with affine motion correction methods in computational feasibility and projection distance. In particular, this allows accurate reconstruction for a proper microscale diamond in the appearance of motion from the practically acquired projection radiographs, which leads to a novel application of 4DCT.

Key words. Iterative tomographic reconstruction, affine motion models, simultaneous motion estimation.

AMS subject classifications. 65K10, 68U10, 68W01, 92C55, 94A08.

1. Introduction. Four-dimensional computed tomography (4DCT) is a crucial aspect of the broader field of CT imaging that captures 3D objects in motion or the changes of the microstructure, or in a more general term, in the evolution of their shape over time. 4DCT reconstruction techniques restore 4D images that can be regarded as changing 3D volumes over time. The reconstruction is based on one or multiple 360° sets of 2D projection images, and applications of 4DCT are widely found in medicine along with materials science, with an expectation of improving the resolution in both spatial and temporal domains [22].

However, object motion during the 4DCT scan introduces motion artefacts in the reconstructed images, if the motion is not taken into account in the reconstruction. These artefacts complicate diagnosis and treatment. Motion-compensating reconstruction techniques have been proposed to eliminate these artifacts and allow accurate reconstruction of the scanned

3D volume [12].

4D tomographic reconstruction methods in the past fifteen years can be categorized into two different groups. The first group of methods imposes restrictions on the spatial and/or temporal domain without parameterizing the motion. Typical examples are total variation regularization (TVR)[21], which encourages sparsity in the spatial domain. Some of the others are spatial-temporal total variation regularization (STTVR)[27], 4D reconstruction using spatial and temporal regularization (4D ROOSTER)[14] and time domain decomposition [18], which additionally aims to encourage sparsity in the temporal domain. Furthermore, in some cases it can be observed that there are local parts in the scanned object that remain static during the entire acquisition. Hence, the region-based simultaneous iterative reconstruction technique (rSIRT)[24] is designed to reconstruct the object and locate the local static regions. Another version makes use of spatial-temporal patch-based regularization [11]. As these methods do not estimate motions, it is challenging to quantify the change of the object during the CT scan no matter what the change is local or global. The other group of methods aim to estimate the motion, most published recently, and is split into two subgroups. The first subgroup consists of methods that estimate general-affine motion parameters directly from projection data (e.g., [26]), whereas the methods in the second subgroup alternate image reconstruction and motion estimation of full deformation vector fields (DVFs) or a limited set of affine motion parameters (e.g., [3, 4, 13, 28, 29]). However, these methods are either not validated on real data or are validated but the optimization strategies rely on the optimizers that require parameter tuning and nested iterations, which increases the computational complexity and reduce the potential acceleration of these algorithms. Furthermore, it is worth noticing that all the methods lack proper study in joint image reconstruction and general affine motion estimation with analytical gradients of the motion towards both the reconstruction and the general affine motion parameters. Although several continuous time-step motion models of simulated objects and discrete-time motion models with a real object are considered as in our previous studies [17, 16, 15], these motion models have not been yet applied to real objects with possibly compatible motion models. Furthermore, quantitative comparisons with state-of-the-art dynamic CT reconstruction methods are currently missing.

Consequently, in this paper, we present an efficient iterative reconstruction and motion correction technique for 4DCT based on the exact gradients of the motion, which can incorporate any parameterizable DVF including general affine motion. Motion models can be deduced either from the characterization of the material of which the object is made, or from the reconstruction without motion correction of the object. Furthermore, we rely on an objective function that depends on both the object volume and the parameterized DVFs, whose gradients towards all these variables are analytically described. This allows simultaneous reconstruction and general affine motion estimation using gradient-based optimization strategies. On the other hand, we extend our findings to real data, followed by quantitative comparisons of the results obtained by our method with the results obtained by the state-of-the-art reconstruction and affine motion estimation methods. In particular, our method allows micro-scale structures of a real diamond whose movement is disruptive for the analysis when using conventional 3DCT reconstruction techniques, which leads to a novel application in 4DCT.

The structure of the rest of the paper is organized as follows: in section 2, we introduce

a mathematical formulation for the 4DCT forward model, in which the CT system operator is inspired by [25, 29] and can be decomposed as the multiplication of the CT projector and the affine motion operator. This is then followed by our underlying algorithm that allows accurate reconstruction and affine motion parameter estimation simultaneously, by considering the corresponding iterative schemes. More specifically, this is a gradient method whose derivatives are given analytically. In section 3, we describe simulated and real projection datasets relevant to the considered motion models, which are used in the validation process in section 4, wherein the comparison with several state-of-the-art methods is given. Another crucial contribution is mentioned in this section is the validation of our method on a real diamond scan, regarded as the very first study in 4DCT that supports diamond inspection. In section 5, we give an overall discussion on the method, followed by a conclusion of the study in section 6. Finally, section 7 provides a future outlook.

2. Proposed method. This section is to provide a mathematical formulation for the affine motions used in dynamic CT processes that study parameterizable DVFs, which allows accurate reconstruction and estimation of the corresponding affine motion parameters. Moreover, a numerical standard is introduced to quantitatively compare the reconstruction and motion estimation results with the results from the state-of-the-art reconstruction and affine motion estimation methods.

2.1. Forward model. A 4D image can be represented as a sequence of $n \geq 2$ 3D images, $\boldsymbol{x}_1, ..., \boldsymbol{x}_n$, each representing the object at a given point in time. Its acquisition can be observed as a collection of subscans, wherein the object is assumed to be static during each subscan. Here, a subscan refers to one or more consecutively acquired projections. This procedure can be mathematically modeled as n systems of linear equations:

$$(2.1) \qquad\qquad \boldsymbol{W}_i \boldsymbol{x}_i = \boldsymbol{b}_i, \text{ for } i = 1, ..., n,$$

where $\boldsymbol{W}_i$ and $\boldsymbol{b}_i$ are the CT projector and the acquired projection data that corresponds to the ith subscan, respectively. These may be represented as the following system:

$$(2.2) \qquad \begin{bmatrix} \boldsymbol{W}_1 & 0 & 0 & 0 \\ 0 & \boldsymbol{W}_2 & 0 & 0 \\ 0 & 0 & \ddots & 0 \\ 0 & 0 & 0 & \boldsymbol{W}_n \end{bmatrix} \begin{bmatrix} \boldsymbol{x}_1 \\ \boldsymbol{x}_2 \\ \vdots \\ \boldsymbol{x}_n \end{bmatrix} = \begin{bmatrix} \boldsymbol{b}_1 \\ \boldsymbol{b}_2 \\ \vdots \\ \boldsymbol{b}_n \end{bmatrix}.$$

Assume that the unknown image $\boldsymbol{x}_i$ of the ith subscan is a transformed version of the unknown static object volume $\boldsymbol{x}$ under a motion model M, which depends on the parameter $\boldsymbol{p}_i$, i.e.,

$$(2.3) \qquad\qquad \boldsymbol{x}_i = M\left(\boldsymbol{p}_i\right) \boldsymbol{x}.$$

Here, $M\left(\boldsymbol{p}_i\right)$ is a linear operator that models the motion as an affine transformation, and the object $\boldsymbol{x}$ is assumed to be static in the first projection(s).

2.2. Analytic derivation of general affine motion operator towards affine motion parameters. By convention, the parameter $\boldsymbol{p}_i$ is the flattened vector that consists of nine elements of the affine matrix $A_i \in \mathbb{R}^{3\times3}$ and three elements of the translation $\boldsymbol{t}_i \in \mathbb{R}^3$ of the following affine transformation:

$$\boldsymbol{x}_i(\boldsymbol{u}) = \boldsymbol{x}(A_i\boldsymbol{u} + \boldsymbol{t}_i). \tag{2.4}$$

The change of the coordinate $\boldsymbol{u}$ of the original image $\boldsymbol{x}$ in the warped image $\boldsymbol{x}_i$ is then a differentiable map towards $\boldsymbol{p}_i$, which is generalized as the following:

$$\widehat{\boldsymbol{u}} = A_i\boldsymbol{u} + \boldsymbol{c} - A_i\boldsymbol{c} + \boldsymbol{t}_i, \tag{2.5}$$

where $\boldsymbol{c} \in \mathbb{R}^3$ is the center of the system of coordinates. Hence, if the motion operator M uses differentiable interpolations (e.g., linear, quadratic or cubic) for the missing coordinates in the warped image, this approach provides an analytic derivative $\nabla M(\boldsymbol{p}_i)\boldsymbol{x}$ for the warped image $M(\boldsymbol{p}_i)\boldsymbol{x}$ towards the affine motion parameter $\boldsymbol{p}_i$ aside an adjoint operator $M(\boldsymbol{p}_i)^T$ [20].

2.3. Dynamic CT model. By decomposing the full stack of transformed images by the relation (2.3) and substituting the result into (2.2), it follows that:

$$\begin{bmatrix} \boldsymbol{W}_1 & 0 & 0 & 0 \\ 0 & \boldsymbol{W}_2 & 0 & 0 \\ 0 & 0 & \ddots & 0 \\ 0 & 0 & 0 & \boldsymbol{W}_n \end{bmatrix} \begin{bmatrix} M(\boldsymbol{p}_1) \\ M(\boldsymbol{p}_2) \\ \vdots \\ M(\boldsymbol{p}_n) \end{bmatrix} \boldsymbol{x} = \begin{bmatrix} \boldsymbol{b}_1 \\ \boldsymbol{b}_2 \\ \vdots \\ \boldsymbol{b}_n \end{bmatrix}, \tag{2.6}$$

or more concisely:

$$\boldsymbol{W}M(\boldsymbol{p})\boldsymbol{x} = \boldsymbol{b}, \tag{2.7}$$

where

$$\boldsymbol{W} = \begin{bmatrix} \boldsymbol{W}_1 & 0 & 0 & 0 \\ 0 & \boldsymbol{W}_2 & 0 & 0 \\ 0 & 0 & \ddots & 0 \\ 0 & 0 & 0 & \boldsymbol{W}_n \end{bmatrix}, \boldsymbol{p} = \begin{bmatrix} \boldsymbol{p}_1 \\ \boldsymbol{p}_2 \\ \vdots \\ \boldsymbol{p}_n \end{bmatrix}, \boldsymbol{M}(\boldsymbol{p}) = \begin{bmatrix} M(\boldsymbol{p}_1) \\ M(\boldsymbol{p}_2) \\ \vdots \\ M(\boldsymbol{p}_n) \end{bmatrix}, \text{ and } \boldsymbol{b} = \begin{bmatrix} \boldsymbol{b}_1 \\ \boldsymbol{b}_2 \\ \vdots \\ \boldsymbol{b}_n \end{bmatrix}. \tag{2.8}$$

2.4. Optimization strategies. In order to solve the non-linear system (2.7) in least-square sense, a modified version of the gradient method in [25, 29] that considers a joint estimation of the motion parameters $\boldsymbol{p}$ along with the image $\boldsymbol{x}$, is used to solve the following minimization problem:

$$[\widehat{\boldsymbol{x}}, \widehat{\boldsymbol{p}}] = \operatorname{argmin}_{\boldsymbol{x},\boldsymbol{p}} f(\boldsymbol{x}, \boldsymbol{p}), \tag{2.9}$$

where

$$f(\boldsymbol{x}, \boldsymbol{p}) = \frac{1}{2} \|\boldsymbol{W}M(\boldsymbol{p})\boldsymbol{x} - \boldsymbol{b}\|_2^2. \tag{2.10}$$

The gradient of this objective function is analytically given by $\nabla f = \left[\left[\nabla_{\boldsymbol{x}} f \right]^T, \left[\nabla_{\boldsymbol{p}} f \right]^T \right]^T$, with

$$(2.11) \qquad \nabla_{\boldsymbol{x}} f\left(\boldsymbol{x}, \boldsymbol{p}\right) = \boldsymbol{M}\left(\boldsymbol{p}\right)^T \boldsymbol{W}^T \boldsymbol{r},$$

and

$$(2.12) \qquad \nabla_{\boldsymbol{p}} f(\boldsymbol{x}, \boldsymbol{p}) = \left[\nabla \boldsymbol{M}\left(\boldsymbol{p}\right) \boldsymbol{x} \right]^T \boldsymbol{W}^T \boldsymbol{r},$$

where $\boldsymbol{r} = \boldsymbol{W} \boldsymbol{M}\left(\boldsymbol{p}\right) \boldsymbol{x} - \boldsymbol{b}$ is the residue of the dynamic CT system.

The implementation of the motion operator $\boldsymbol{M}\left(\boldsymbol{p}\right)$, its adjoint $\boldsymbol{M}\left(\boldsymbol{p}\right)^T$ and its derivative $\nabla \boldsymbol{M}\left(\boldsymbol{p}\right)$ are all done beforehand by the ImWIP [19]- an open-source warping toolbox that contains matrix-free and GPU-accelerated implementations of cubic image warping, its adjoint and its analytical derivatives. The projector $\boldsymbol{W}$ and its adjoint $\boldsymbol{W}^T$ are provided by the ASTRA Toolbox [23].

In theory, an ordinary update step using a gradient method would require a single step size γ^k to be chosen for the update of both the image and the motion parameters:

$$(2.13) \qquad \left(\boldsymbol{x}^{k+1}, \boldsymbol{p}^{k+1} \right) = \left(\boldsymbol{x}^k, \boldsymbol{p}^k \right) - \gamma^k \nabla f \left(\boldsymbol{x}^k, \boldsymbol{p}^k \right).$$

However, to accommodate for the fact that the motion parameters play a fundamentally different role in the system, and that they influence the objective function with different sensitivities, the update of the gradient method is split in their corresponding parts with an independent stepsize for each part:

$$(2.14) \qquad \boldsymbol{x}^{k+1} = \boldsymbol{x}^k - \gamma_{\boldsymbol{x}}^k \nabla_{\boldsymbol{x}} f \left(\boldsymbol{x}^k, \boldsymbol{p}^k \right),$$

and

$$(2.15) \qquad \boldsymbol{p}^{k+1} = \boldsymbol{p}^k - \gamma_{\boldsymbol{p}}^k \nabla_{\boldsymbol{p}} f \left(\boldsymbol{x}^k, \boldsymbol{p}^k \right).$$

If more than one motion model is considered, the scheme (2.15) is split up even further. Specifically, let us consider an affine motion that describes either rigid motions (rotations $\boldsymbol{\theta}$, translations $\boldsymbol{t}$) or non-rigid motions (scalings $\boldsymbol{s}$, etc), then

$$(2.16) \qquad \boldsymbol{\theta}^{k+1} = \boldsymbol{\theta}^k - \gamma_{\boldsymbol{\theta}}^k \nabla_{\boldsymbol{\theta}} f \left(\boldsymbol{x}^k, \boldsymbol{\theta}^k, \boldsymbol{t}^k, \boldsymbol{s}^k, \dots \right),$$

$$(2.17) \qquad \boldsymbol{t}^{k+1} = \boldsymbol{t}^k - \gamma_{\boldsymbol{t}}^k \nabla_{\boldsymbol{t}} f \left(\boldsymbol{x}^k, \boldsymbol{\theta}^k, \boldsymbol{t}^k, \boldsymbol{s}^k, \dots \right),$$

$$(2.18) \qquad \boldsymbol{s}^{k+1} = \boldsymbol{s}^k - \gamma_{\boldsymbol{s}}^k \nabla_{\boldsymbol{s}} f \left(\boldsymbol{x}^k, \boldsymbol{\theta}^k, \boldsymbol{t}^k, \boldsymbol{s}^k, \dots \right), \text{ and so on.}$$

If the size of the object volumes and the number of subscans are not too large, the stepsizes $\gamma_{\boldsymbol{x}}^k$ and $\gamma_{\boldsymbol{p}}^k$ in the first iterations can be chosen by a backtracking line search until the Armijo condition [1] is fulfilled, and the line search can be executed on typical computers [16]. On the other hand, the line search strategies become impractical for higher scale volumes, but empirically these stepsizes can be chosen by a smaller proportion of the normalized values

$1/\|\nabla_\square f\|_2$ by suitable proportional coefficients $c_\square^0$, i.e., $\gamma_\square^0 = c_\square^0/\|\nabla_\square f\|_2$. After which, the Barzilai-Borwein formula [2] is used in the following iterations, which exploits the information of the entire scan and provides an accelerated convergence speed compared with the line search strategies [9] for the schemes (2.14) and (2.15):

$$(2.19) \qquad \mu_\square^k = \frac{\langle \nabla_\square f\left(\boldsymbol{x}^k, \boldsymbol{p}^k\right) - \nabla_\square f\left(\boldsymbol{x}^{k-1}, \boldsymbol{p}^{k-1}\right), \square^k - \square^{k-1}\rangle}{\|\nabla_\square f\left(\boldsymbol{x}^k, \boldsymbol{p}^k\right) - \nabla_\square f\left(\boldsymbol{x}^{k-1}, \boldsymbol{p}^{k-1}\right)\|^2}, \text{ where } \square = \boldsymbol{x} \text{ or } \boldsymbol{p}.$$

Because of the large scale of the 3D object volume sizes, it is challenging to directly implement the formulas (2.11) and (2.12). Nonetheless, the objective function (2.10) can be rewritten as follows in the sparsity property of the projection operator $\boldsymbol{W}$:

$$(2.20) \qquad f\left(\boldsymbol{x}, \boldsymbol{p}\right) = \frac{1}{2} \|\boldsymbol{W}\boldsymbol{M}(\boldsymbol{p})\boldsymbol{x} - \boldsymbol{b}\|_2^2$$

$$(2.21) \qquad = \frac{1}{2} \left\| \begin{bmatrix} \boldsymbol{W}_1 & 0 & 0 & 0 \\ 0 & \boldsymbol{W}_2 & 0 & 0 \\ 0 & 0 & \ddots & 0 \\ 0 & 0 & 0 & \boldsymbol{W}_n \end{bmatrix} \begin{bmatrix} M(\boldsymbol{p}_1) \\ M(\boldsymbol{p}_2) \\ \vdots \\ M(\boldsymbol{p}_n) \end{bmatrix} \boldsymbol{x} - \begin{bmatrix} \boldsymbol{b}_1 \\ \boldsymbol{b}_2 \\ \vdots \\ \boldsymbol{b}_n \end{bmatrix} \right\|_2^2$$

$$(2.22) \qquad = \frac{1}{2} \left\| \begin{bmatrix} \boldsymbol{W}_1 M(\boldsymbol{p}_1)\boldsymbol{x} - \boldsymbol{b}_1 \\ \boldsymbol{W}_2 M(\boldsymbol{p}_2)\boldsymbol{x} - \boldsymbol{b}_2 \\ \vdots \\ \boldsymbol{W}_n M(\boldsymbol{p}_n)\boldsymbol{x} - \boldsymbol{b}_n \end{bmatrix} \right\|_2^2$$

$$(2.23) \qquad = \frac{1}{2} \sum_{i=1}^n \|\boldsymbol{W}_i M\left(\boldsymbol{p}_i\right) \boldsymbol{x} - \boldsymbol{b}_i\|_2^2 .$$

The partial derivative towards the reconstruction (2.11) is then given by:

$$(2.24) \qquad \nabla_{\boldsymbol{x}} f\left(\boldsymbol{x}, \boldsymbol{p}\right) = \sum_{i=1}^n M\left(\boldsymbol{p}_i\right)^T \boldsymbol{W}_i^T \left[\boldsymbol{W}_i M\left(\boldsymbol{p}_i\right) \boldsymbol{x} - \boldsymbol{b}_i\right].$$

Similarly, the partial derivative towards each parameter based on the general form as given by the equation (2.12), is given as follows:

$$(2.25) \qquad \nabla_{\boldsymbol{p}_i} f(\boldsymbol{x}, \boldsymbol{p}) = \left[\nabla M\left(\boldsymbol{p}_i\right) \boldsymbol{x}\right]^T \boldsymbol{W}_i^T \left[\boldsymbol{W}_i M\left(\boldsymbol{p}_i\right) \boldsymbol{x} - \boldsymbol{b}_i\right],$$

which is an invariant to the motion parameters corresponding to the other subscans.

It is important to note that the objective function f is *non-convex* towards the motion parameters $\boldsymbol{p}$. Moreover, the objective function does not always decrease due to the instability of the Barzilai-Borwein method. To the best of our knowledge, up to now, there has not been a mathematical proof of the convergence of the iterative schemes (2.14) and (2.15). Nonetheless, the convergence has been empirically verified in [17, 16, 15].

We will call the *reconstruction without motion correction* to be the reconstruction obtained by executing the scheme (2.14) when the motion operator is not taken into account. This

is a useful initial guess for MIRT with respect to the optimization and on the other hand particularly the solution to the following minimization problem:

$$(2.26) \qquad \boldsymbol{x}^0 = \mathrm{argmin}_{\boldsymbol{x}} \|\boldsymbol{W}\boldsymbol{x} - \boldsymbol{b}\|_2^2,$$

which can be solved by any least-square solver (e.g., LSQR, BFGS, or GM-BB (gradient method with the stepsizes computed by the Barzilai-Borwein formula)).

The following metric is used to evaluate the quality of the 4DCT techniques:

Definition 2.1. *Let $\widehat{\boldsymbol{b}}_i$ and $\boldsymbol{b}_i$ be the re-projection with estimated motion parameters before-hand and the projection data in the real acquisition, respectively. The projection distance is the quantity defined by*

$$(2.27) \qquad PD = \left\|\widehat{\boldsymbol{b}}_i - \boldsymbol{b}_i\right\|_2.$$

In particular, for MIRT the PD is given as:

$$(2.28) \qquad PD = \|\boldsymbol{W}_i M\left(\widehat{\boldsymbol{p}}_i\right)\widehat{\boldsymbol{x}} - \boldsymbol{b}_i\|_2,$$

where $\widehat{\boldsymbol{x}}$ and $\widehat{\boldsymbol{p}}_i$ are the simultaneous reconstruction and the motion parameters corresponding to the ith projection, respectively.

3. Datasets. In this section, we describe several datasets used for testing our method. Synthetic datasets were simulated by the ASTRA Toolbox [23] and the ImWIP [19], and real datasets were acquired by the TESCAN UniTOM XL systems at either the UAntwerpen Center for 4D Quantitative X-ray Imaging and Analysis[1] or the KU Leuven XCT Core Facility[2]. The projection geometry in all real scans is cone beam. The flat field correction and log normalization were all done by the FlexRayTools [6].

3.1. Real sponge dataset. The dataset consists of projections acquired from two consecutive stop-and-shoot full angular-range cone-beam scans with chosen projection angles in the first and second scans are $[0, \pi)$ and $[\pi, 2\pi)$, respectively. The voxel size was set to be 92.46 (μm). The projection setting parameters $SOD = 462$ (mm) and $SDD = 750$ (mm), and the pixel size of the detector was set to be 0.15 (mm).

In particular, the sponge was static in the first full scan, and vertically compressed in the second full scan with the scaling factor in 3D is $\widehat{\boldsymbol{s}} = (s_x, s_y, s_z) = (0.97, 0.93, 1.21)$, which is estimated by solving the following problem:

$$(3.1) \qquad \widehat{s} = \mathrm{argmin}_{\boldsymbol{s}} \|M(\boldsymbol{s})\boldsymbol{x}_1 - \boldsymbol{x}_2\|_2^2,$$

where $\boldsymbol{x}_1$ and $\boldsymbol{x}_2$ are the reconstruction of the sponge from the projection data acquired in the first and the second full scans, respectively. Here, the reconstruction $\boldsymbol{x}_1$ can be used as a ground truth object for validating any 4DCT reconstruction on this dataset.

---

[1]https://www.uantwerpen.be/en/research-facilities/center-for-4d-quantitative-x-ray/
[2]https://xct.kuleuven.be/

3.2. Real bone scaffold dataset. The dataset was created by extracting projection data from a continuous acquisition in-situ compression experiment with dynamic loading a bone scaffold, acquired in 6 continuous full angular scans. More specifically, the extraction was performed by merging data from 6 adjacent cone-beam geometries of projection angles. The obtained voxel size after 2×2 binning of the detector of the size 1896×1920 (pixel) is 37 μm. By taking 720 projections over a $360°$ rotation, a temporal resolution of 29 seconds is achieved. The projection setting parameters $SOD = 70$ (mm) and $SDD = 850$ (mm), and the pixel size of the detector was set to be 0.45 (mm).

3.3. Real diamond dataset. The real projection dataset is used for validating the reconstruction with rigid motion compensation. The cone-beam acquisition consists of a full equilateral angular range of 2879 projections of the size 1896×1920 (pixel) of a real round diamond (Figure 8), whose diameter is measured geometrically from the projection data and the projection geometry to be 12.376 mm (around 7.3 carats). The voxel size was achieved to be 8 μm. The projection setting parameters $SOD = 40$ (mm) and $SDD = 750$ (mm), and the pixel size of the detector was set to be 0.15 (mm).

3.4. Simulated diamond phantom. A homogeneous diamond phantom of the size $320 \times 320 \times 320$ (voxel) was obtained by voxelizing an approximate surface mesh of the reconstruction without motion correction of the diamond from the real projection dataset described in subsection 3.3. The surface mesh was created using the *Volume to Mesh* modifier in Blender [5], followed by a remeshing operation. A visualization of the binary diamond phantom is presented in Figure 6.

4. Experiments. In this section, we test our proposed method on the datasets described in section 3. MIRT and the Cryo-EM reconstruction method [29] were tested on the same computer with the following hardware configuration: Intel® Core™ i7, RAM 64 GB, GPU GeForce RTX 2080 SUPER working on Linux OS. [26] was tested on a computer with similar hardware configuration but with a GPU GeForce RTX 1070 and Windows OS. Afterwards, we compare the results obtained by our method with the results obtained by the relevant affine-motion estimation methods [26, 29]. Because only affine motion parameters corresponding to the deformations perpendicular to the projection direction are accurately estimated, we do not compare estimated motion parameters with the ground truth parameters in the simulation experiments.

4.1. Scaling motion estimation. Our proposed method is tested on several datasets acquired by capturing objects in scaling, including the real sponge and the real bone scaffold datasets described in subsection 3.1 andsubsection 3.2, respectively.

4.1.1. Experiment on simulated projection dataset. We consider a 3D natural breathing motion model that consists of 5 cycles, as an extension of the 2D case presented in [16]. The object is the 3D Shepp-Logan phantom of the size $128 \times 128 \times 128$ (voxel) provided by the TomoPy [8], and the true scaling factor s_i at the ith time point is given by:

$$(4.1) \qquad s_i = 1 - 0.2 \sin\left(5 \times \frac{2\pi \times i}{128}\right).$$
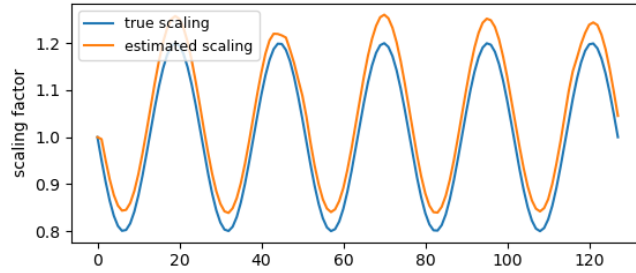
Figure 1: scaling parameter estimation result of the simulation experiment on the 3D Shepp-Logan phantom (horizontal axis: i^{th} subscan).

The projection geometry is cone beam. The projection setting parameters $SOD = 500$ (voxel) and $ODD = 150$ (voxel). The distance between the centers of two horizontally and vertically adjacent detector pixels was set to be 1 (mm), and the detector size was set to be 192×192 (pixel). Gaussian noise with a standard deviation of 1% of the peak gray value of the projection data was added to the sinogram. The estimated scaling parameters are given in Figure 1, and the reconstruction results are given in Figure 2.

4.1.2. Experiment on the sponge's real projection dataset. To validate the scaling estimation so that a consistent quantitative comparison with [26] can be made, 16 angular-ranged projections of the sponge acquired in the first full real scan and a projection acquired in the second full real scan, were used to be the data of the first and second subscans of the dynamic scan. The object volume size was set to be $474 \times 480 \times 480$ (voxel) and the results on the projection difference were cropped to the object area for better visualization. The stopping criterium of [26] was used according to the default setting of the method's authors. To achieve convergence in this case, 10 iterations of MIRT were needed. Results on the projection distance, shown in Figure 3 indicates that MIRT outperforms [26].

4.1.3. Experiment on the bone scaffold's real projection dataset. The projections were cropped to the smaller size of 250×250 (pixel) that sufficiently covered the projections of the object area. The object volume size was set to be $250 \times 250 \times 250$ (voxel). The reconstruction from the projection data of the first full angular scan was set as reference object presented in Figure 5 for visual comparison. To validate MIRT, we ran 300 iterations and the computation speed recorded was around 6 (sec./iter.). The proportional coefficients for the intial stepsizes of the reconstruction and scaling estimation schemes are $c_{\boldsymbol{x}}^0 = 1$ and $c_{\boldsymbol{s}}^0 = 0.1$, respectively. The reconstruction results are shown in Figure 5.

4.2. Rigid motion estimation. Our proposed method is tested on the acquisition of solid objects, including simulated projection data of the homogeneous diamond phantom and real projection data of the real diamond described in subsection 3.4 and subsection 3.3, respectively.

4.2.1. On the homogeneous diamond phantom: simulation experiment 1. This sub-section provides a consistent experiment setup so that our method can be compared with [26]. The object volume was slightly cropped to be of the size $300 \times 310 \times 320$ (voxel). 8 projections

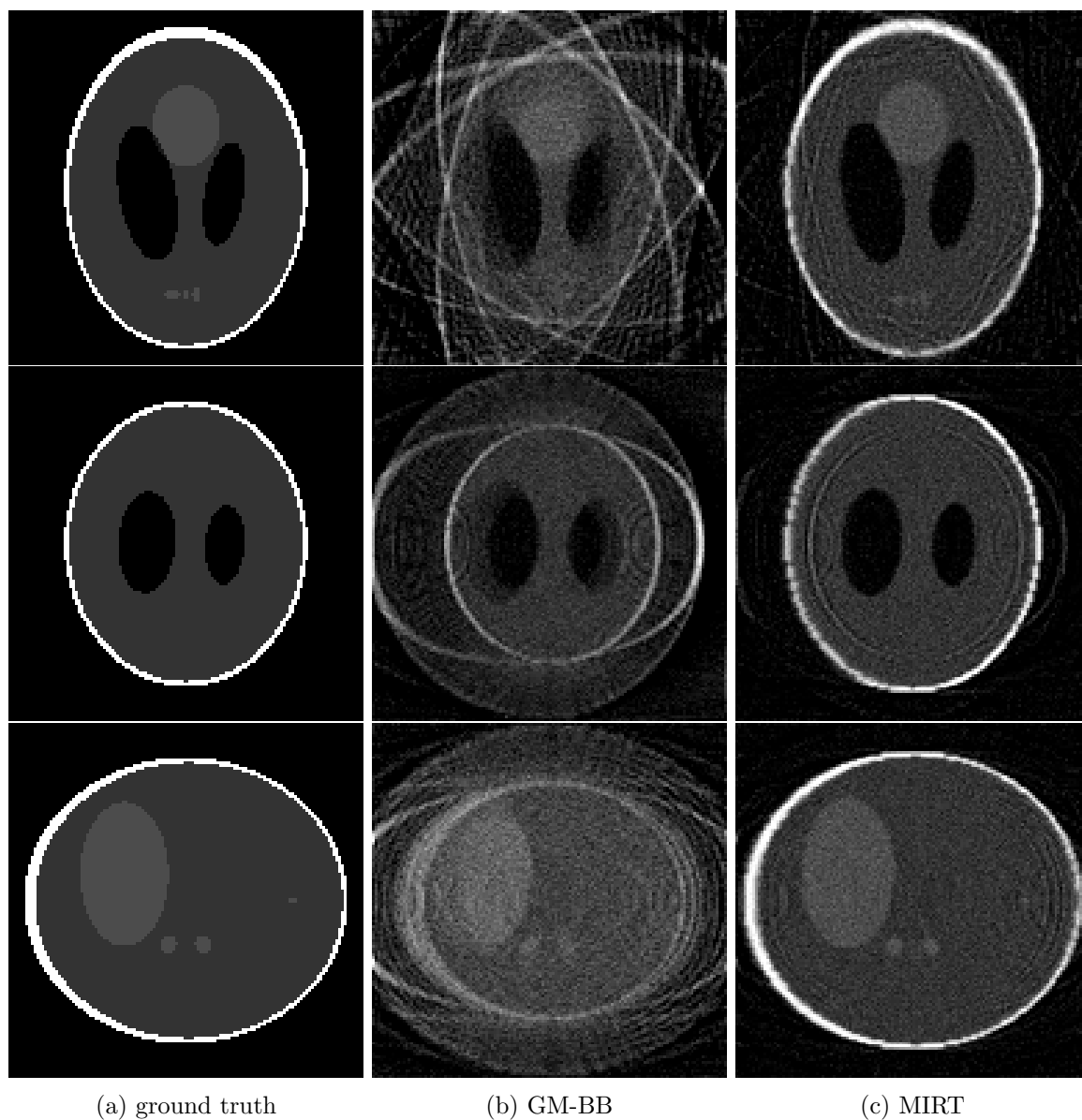(a) ground truth   (b) GM-BB   (c) MIRT

Figure 2: central cross-sections of the reconstruction results on the 3D Shepp-Logan phantom.

were used in the reference scan for the method [26], followed by a projection chosen in the main scan in which the object was translated in three dimensions with the corresponding displacement $[-5, 7, 10]$ (voxel), and was rotated with the corresponding angles $[0.02, -0.05, 0.1]$ (rad). Gaussian noise with a standard deviation of 1% of the peak gray value of the projection data was added to the sinogram. MIRT quickly converged after 10 iterations with a

(a) without scaling correction:
$PD = 28.84$.

(b) with general affine correction [26]:
$PD = 25.63$.

(c) with scaling-restricted correction [26]:
$PD = 25.33$.

(d) with MIRT: $PD = 9.68$.
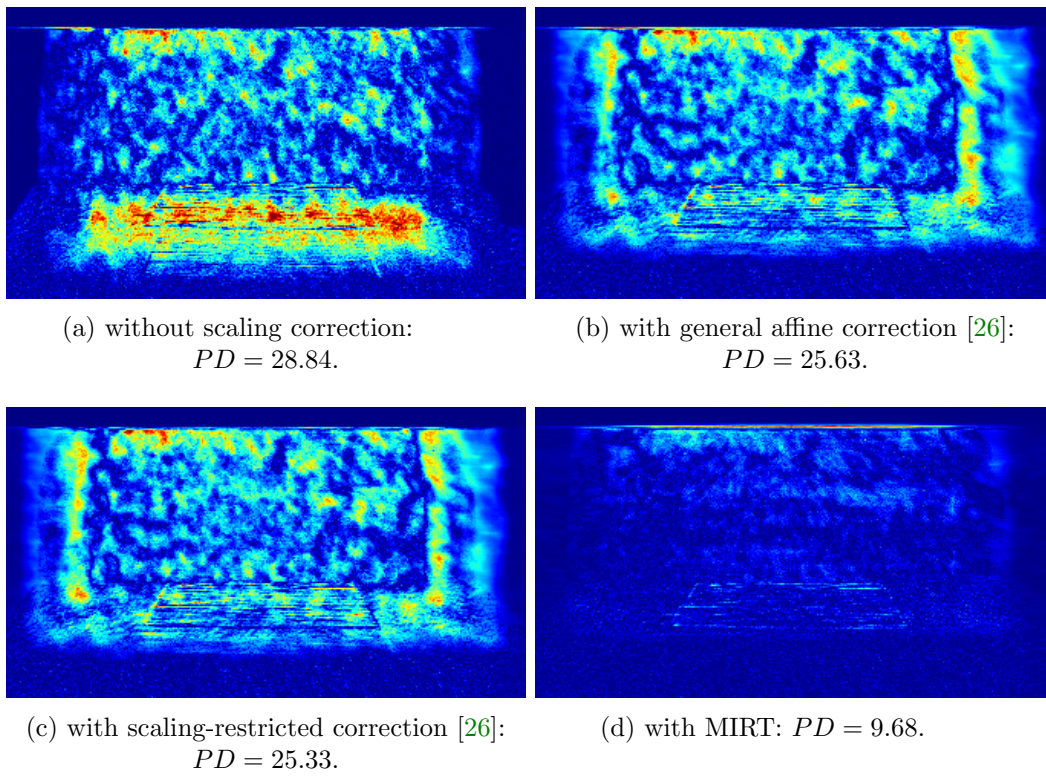
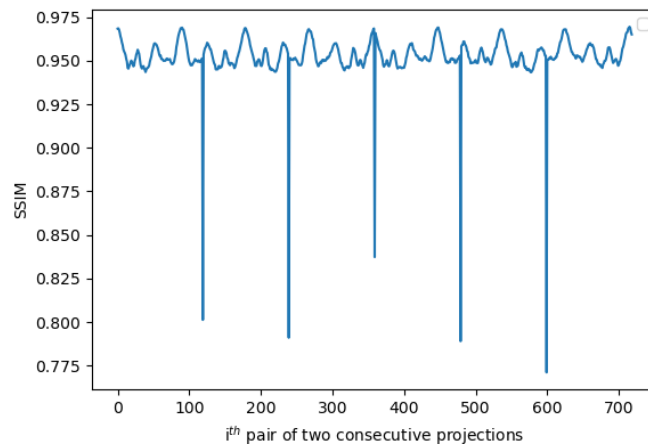Figure 3: projection differences and projection distances (PD) results on the sponge's real projection data.

Figure 4: SSIM values of successive projections of the bone scaffold's real projection data tested in the experiment.
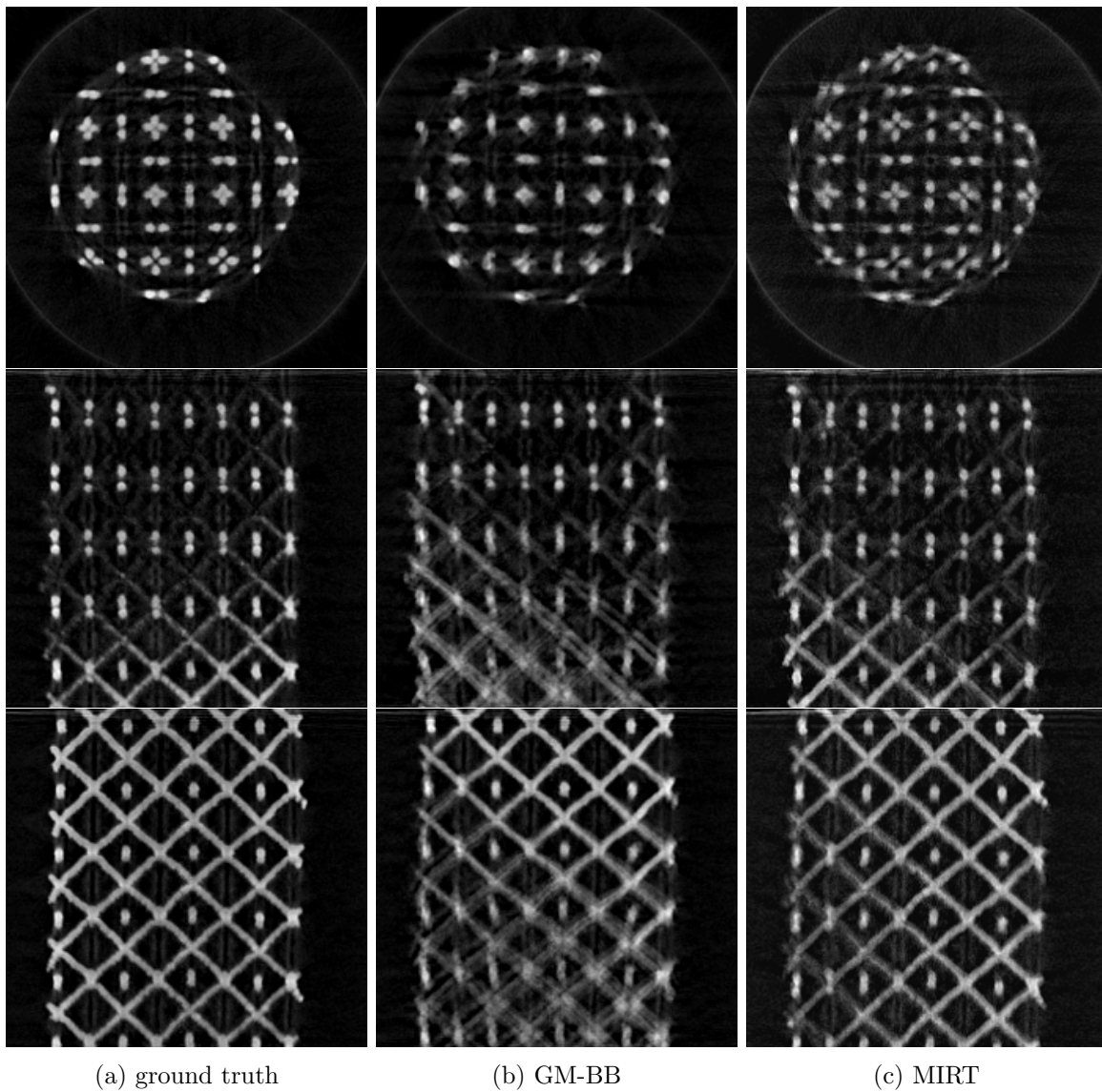
| (a) ground truth | (b) GM-BB | (c) MIRT |

Figure 5: central cross-sections of the reconstruction results on the bone scaffold's real projection data.

running speed less than 4 sec./iter. An example of the projection differences is presented in the Figure 7, in which MIRT outperforms [26] in projection distance.

4.2.2. On the homogeneous diamond phantom: simulation experiment 2. This subsection provides a consistent experiment setup so that our method can be compared with [29]. Considering a continuous motion estimation on the homogeneous diamond volume size $320 \times 320 \times 320$ (voxel) that was acquired in a full-angular scan that contained 10 equilat-
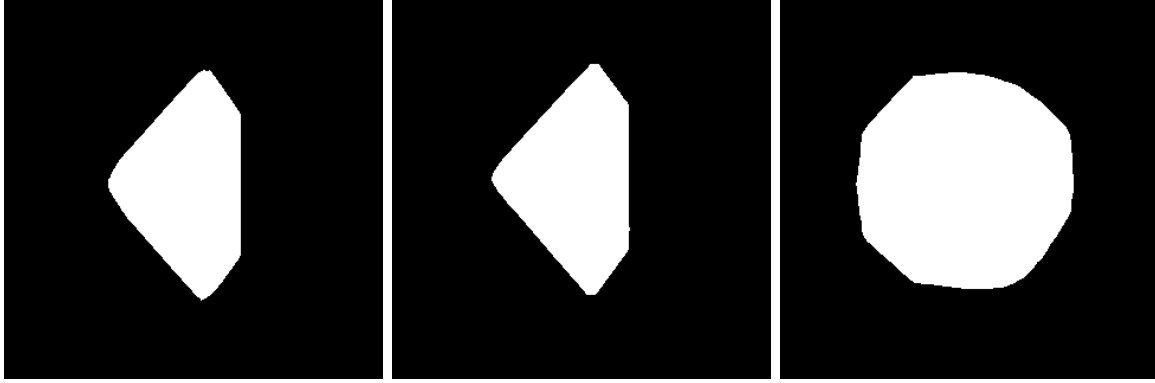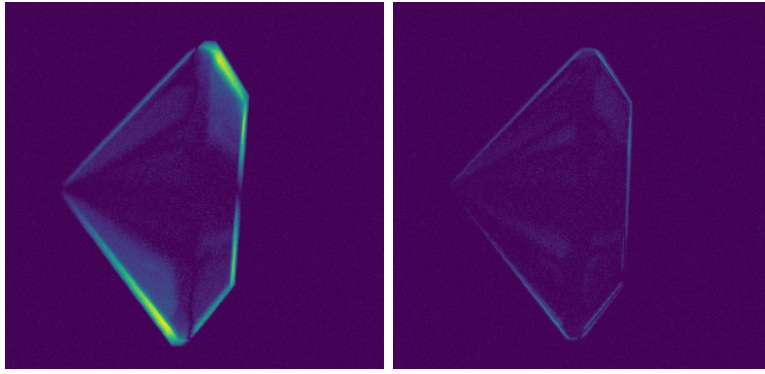
Figure 6: central cross-sections of the 3D homogeneous diamond phantom.

(a) with [26]: $PD = 3107.95$.   (b) with MIRT: $PD = 944.77$.

Figure 7: projection distances on the first projection of the homogeneous diamond phantom.

eral projection angles, each GD step update implemented by [29] took more than 10 minutes and the same time for 200 iterations of the ADMM optimizer executed in the same method, when each iteration of MIRT with the parallel beam geometry (consistently with the Cryo-EM reconstruction technique [29]) took around 35 seconds by running on the same computer.

4.2.3. Experiment on the real diamond dataset. The binning number was set to four to downscale the projections to the size 472×480 (pixel), which is large enough for the motion artefacts being visually visible in the reconstruction without motion correction. The object volume size is set to be $472 \times 480 \times 480$ (voxel). It can be seen from the visualization of the difference between the first and the last projections in Figure 9 that the diamond was in motion during the scan. To estimate this movement by using MIRT, 90 iterations were used with the proportional coefficients for the initial stepsizes of the reconstruction, rotation and translation estimation schemes are $c_{\boldsymbol{x}}^0 = 1$, $c_{\theta}^0 = 0.001$ and $c_{\boldsymbol{t}}^0 = 0.1$, respectively. The computation speed was recorded to be around 60 (sec./iter.). On the other hand, [29] cannot

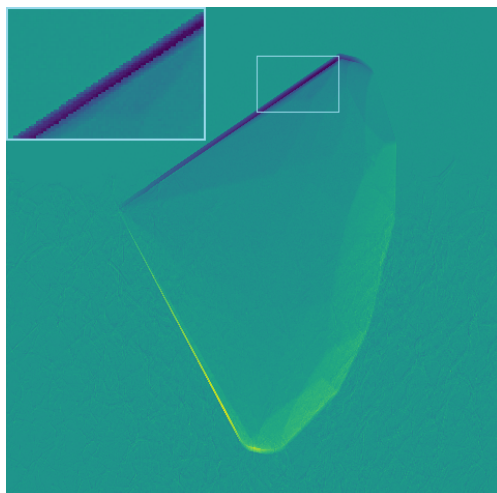Figure 8: the real diamond in front of the X-ray source of the CT scanner.

Figure 9: difference of the projections at the initial projection angle and the last projection angle of the real diamond.

handle the given object volume size due to memory limitations.

The reconstruction with compensation of rigid motion artefacts of the real diamond are shown in Figure 10, in which the misalignment in the reconstruction without motion correction are corrected in the reconstruction results obtained by MIRT.

5. Discussion. The results on both simulation and real experiments clearly show an improvement of our method in comparison with GD-BB, which does not take into account the motion estimation. On the other hand, our method is validated on several real datasets when most of the state-of-the-art methods [3, 4, 26, 13, 28, 29] have not attempted yet. Further-
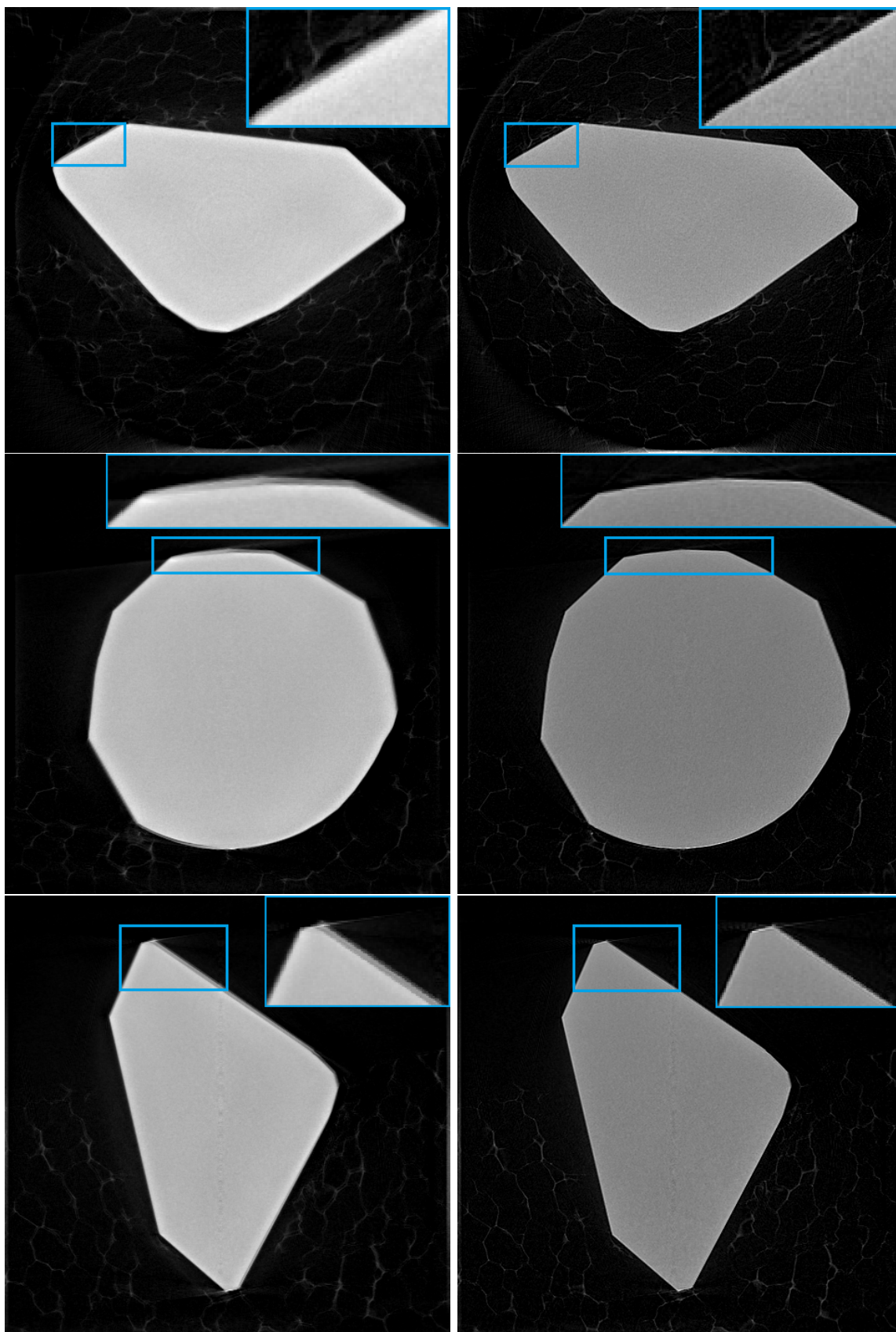
(a) GD-BB   (b) MIRT

Figure 10: central cross-sections of the reconstruction results on the real diamond dataset.

more, the methods [26, 13] are tested on real datasets, but nested iterations complicate the computation. In particular, our method outperforms the two relevant CT reconstruction and affine motion correction techniques [26, 29] in computational feasibility and [26] in projection distance.

Every methods have pros and cons, and our method is not an exceptional case. Despite the success of the validation on both simulated and real data, a mathematical proof for the convergence of iterative schemes (2.14) and (2.15) is currently still missing due to the non-convexity of the proposed objective function towards the affine motion parameters. On the other hand, we ran as many iterations as possible and kept an eye until the convergence is achieved instead of setting a specific stopping criterion, which will be studied in future research.

6. Conclusion. We have presented a mathematical method for 4DCT that allows accurate reconstruction and affine motion correction. As for the shown results, our approach emphasizes practical applicability in areas where current state-of-the-art methods fall short. Specifically, our method surpasses existing 4DCT reconstruction and affine motion correction techniques in terms of computational feasibility and residual errors. The findings are consistent among experiments on both synthetic and real datasets, and highlight a new application for 4DCT for higher resolving 3DCT reconstructions, as the state-of-the-art would allow. Another of our main contributions is that this outputs an accurate reconstruction with the rigid motion artefacts compensated for a real diamond in which MIRT clearly gives better reconstructions in case of motion, which directly results in a novel application of 4DCT.

7. Future work. In this study, we parameterized the rotation by using not only the conventional Euler angles but also the Cayley transforms of these that eliminate the uncommutativity of the rotations along the three axes. Although these traditional approaches have been very efficient, there does exists an inconvenience relevant to the computational cost. In the future, we aim to overcome this disadvantage by developing for the affine motion operators a parameterization using the Lie algebras whose computation efficiency was mathematically proved [10], and designing a parallelization strategy for estimating the motion at each projection. Moreover, the problem of how to choose suitable subscans will be further studied (an insight of the strategy is shortly introduced at the appendix below).

Data availability. Data can be made available upon request.

Appendix: determination of feasible subscans. Although the method has been empirically validated on both simulated and real projection datasets, the choice for the best subscans still remains an open question. This section does not give an exact solution to the problem but provides an insight in choosing such subscans so that the method works with an improved performance.

The trivial fact is that the choice of feasible subscans strongly depend on the data. In theory, one needs to determine at which projection there is more motion than the previous [7]. More specifically, if the subscans are of an equal size, the method performs well in estimating monotone motions. However, if the motion is more complicated (e.g., natural breathing), continuous motion estimation must be considered.

Because the object is assumed to be static in each subscan, there should be no significant

differences between the metric values of the pairs of two successive projections within. For instance, it can be seen from the Figure 4 that there are five points dropped in the SSIM values, which results in six subscans that are chosen for validating the scaling estimation on the bone scaffold's real projection dataset.

In order to study the problem in a general case, let us consider a dynamic full scan consists of $N + 1$ projections $\boldsymbol{y}_1, \boldsymbol{y}_2, \ldots, \boldsymbol{y}_{N+1}$.

Definition 7.1 (feasible subscan). *A subscan is said to be feasible if there is not a significant change of the object through the projections within it. In other words, the pairs of two adjacent projections within it are relatively approximated in any specific metric.*

The problem *feasible subscan partition* of projections can be mathematically formulated using the SSIM metric as the following:

Problem 1 (feasible subscan partition). *Let $\boldsymbol{s} = [s_1, s_2, \ldots, s_N]^T \in [0, 1]^N$ be a vector that collects the SSIM values of all pairs of two adjacent projections. More specifically,*

$$(7.1) \qquad s_i = SSIM(\boldsymbol{y}_i, \boldsymbol{y}_{i+1}), \forall i = \overline{1, N}.$$

One needs to partition the finite set $\mathcal{S} = \{1, 2, 3, \ldots, N\}$ into n mutually exclusive subsets $\mathcal{S}_1, \mathcal{S}_2, \ldots$ and $\mathcal{S}_n$, in which each contains consecutive integers so that the projections corresponding to the same subset of indices are similar under SSIM standard. Mathematically speaking, for any integer k such that $1 \leq k \leq n$, the following inequality holds for a given specific value ϵ:

$$(7.2) \qquad |s_i - s_j| < \epsilon, \ \forall i, j \in \mathcal{S}_k.$$

On the other hand, in order to reduce the complexity of the computation (2.20), the optimal value of the number of feasible subscans must be minimized. As a result, it yields the following statistical integer programming problem:

$$(7.3) \qquad [\widehat{n}, \widehat{\sigma}_1, \ldots, \widehat{\sigma}_{\widehat{n}}] = \underset{n, \sigma_1, \ldots, \sigma_n}{\arg\min} g(n, \sigma_1, \ldots, \sigma_n),$$

with

$$(7.4) \qquad g(n, \sigma_1, \ldots, \sigma_n) = n + \lambda \sum_{k=1}^{n} \sigma_k^2,$$

where $\sigma_k^2 = Var(\{s_l | l \in \mathcal{S}_k\}) \in [0, 1]$, and $\lambda > 0$ is the trade-off coefficient between the integer term and the statistical term.

Theorem 7.2. *Solution(s) to the problem "feasible subscan partition" exist only when the trade-off coefficient $\lambda > 1$.*

Proof. Let us consider the contradictory assumption $\lambda \leq 1$. Assume that the projections are partitioned into $\widehat{n} \geq 2$ feasible subscans. Evidently, the variance of the SSIM values satisfies $0 \lesssim \widehat{\sigma}_i^2 \leq 1 \ \forall i = \overline{1, \widehat{n}}$ due to the boundedness of the chosen metric. As a result, if $\widehat{n} \geq 2$ then it yields:

$$(7.5) \qquad g(\widehat{n}, \widehat{\sigma}_1, \ldots, \widehat{\sigma}_n) = \widehat{n} + \lambda \sum_{k=1}^{n} \widehat{\sigma}_k^2 \geq 2 \geq 1 + \lambda\widehat{\sigma}^2,$$

which is the value of the objective function if and only if there is the subscan identical to the full scan, i.e., $\widehat{n} \equiv 1$ and $\widehat{\sigma}^2 \equiv Var\left(\{s_i | i \in \mathcal{S}\}\right)$. This contradiction demonstrates the negation of the contradictory assumption. ∎

REFERENCES

[1] L. ARMIJO, *Minimization of functions having Lipschitz continuous first partial derivatives*, Pacific Journal of Mathematics, 16 (1966), pp. 1–3.

[2] J. BARZILAI AND J. BORWEIN, *Two-point step size gradient methods*, IMA Journal of Numerical Analysis, 8 (1988), pp. 141–148.

[3] C. CHEN, B. GRIS, AND O. ÖKTEM, *A new variational model for joint image reconstruction and motion estimation in spatiotemporal imaging*, SIAM Journal on Imaging Sciences, 12 (2019), pp. 1686–1719.

[4] J. CHUNG AND L. NGUYEN, *Motion estimation and correction in photoacoustic tomographic reconstruction*, SIAM Journal on Imaging Sciences, 10 (2017), pp. 216–242.

[5] B. O. COMMUNITY, *Blender - a 3D modelling and rendering package*, Blender Foundation, Stichting Blender Foundation, Amsterdam, 2018, http://www.blender.org.

[6] B. DE SAMBER, J. RENDERS, T. ELBERFELD, Y. MARIS, J. SANCTORUM, N. SIX, Z. LIANG, J. DE BEEN-HOUWER, AND J. SIJBERS, *FleXCT: a flexible X-ray CT scanner with 10 degrees of freedom*, Optics Express, 29 (2021), pp. 3438–3457.

[7] S. ENS, J. ULRICI, E. HELL, AND T. M. BUZUG, *Automatic detection of patient motion in cone-beam computed tomography*, in 2010 IEEE International Symposium on Biomedical Imaging: From Nano to Macro, 2010, pp. 1257–1260.

[8] D. GÜRSOY, F. DE CARLO, X. XIAO, AND C. JACOBSEN, *TomoPy: a framework for the analysis of synchrotron tomographic data*, Journal of Synchrotron Radiation, 21 (2014), p. 1188–1193.

[9] P. C. HANSEN, J. JØRGENSEN, AND W. R. B. LIONHEART, *Computed Tomography: Algorithms, Insight, and Just Enough Theory*, Society for Industrial and Applied Mathematics, 2021.

[10] S. KAJI AND H. OCHIAI, *A concise parametrization of affine transformation*, SIAM Journal on Imaging Sciences, 9 (2016), pp. 1355–1373.

[11] D. KAZANTSEV, W. M. THOMPSON, W. R. B. LIONHEART, G. V. EYNDHOVEN, A. P. KAESTNER, K. J. DOBSON, P. J. WITHERS, AND P. D. LEE, *4D-CT reconstruction with unified spatial-temporal patch-based regularization*, Inverse Problems and Imaging, 9 (2015), pp. 447–467.

[12] S. S. KORREMAN, *Motion in radiotherapy: photon therapy*, Physics in Medicine & Biology, 57 (2012), p. R161.

[13] F. LUCKA, N. HUYNH, M. BETCKE, E. ZHANG, P. BEARD, B. COX, AND S. ARRIDGE, *Enhancing compressed sensing 4D photoacoustic tomography by simultaneous motion estimation*, SIAM Journal on Imaging Sciences, 11 (2018), pp. 2224–2253.

[14] C. MORY, V. AUVRAY, B. ZHANG, M. GRASS, D. SCHÄFER, S. J. CHEN, J. D. CARROLL, S. RIT, F. PEYRIN, P. DOUEK, AND L. BOUSSEL, *Cardiac C-arm computed tomography using a 3D + time ROI reconstruction method with spatial and temporal regularization*, Medical Physics, 41 (2014), p. 2.

[15] A.-T. NGUYEN, J. RENDERS, J. SIJBERS, AND J. DE BEENHOUWER, *Region-based motion-corrected iterative reconstruction technique for dynamic computed tomography*, in IEEE International Symposium on Biomedical Imaging (ISBI), Cartagena de Indias, Colombia, 2023.

[16] A.-T. NGUYEN, J. RENDERS, J. SOETE, M. WEVERS, J. SIJBERS, AND J. DE BEENHOUWER, *An accelerated motion-compensated iterative reconstruction technique for dynamic computed tomography*, in Proc. SPIE 12242, Developments in X-Ray Tomography XIV, 122421F, San Diego, CA, United States, 2022.

[17] A.-T. Nguyen, J. Renders, J. Soete, M. Wevers, J. Sijbers, and J. De Beenhouwer, *Analytic derivatives of scaling motion-compensated projection operators for dynamic computed tomography*, e-Journal of Nondestructive Testing, 27 (2022), p. 1–5.

[18] V. V. Nikitin, M. Carlsson, F. Andersson, and R. Mokso, *Four-dimensional tomographic reconstruction by time domain decomposition*, IEEE Transactions on Computational Imaging, 5 (2019), pp. 409–419.

[19] J. Renders, B. Jeurissen, A.-T. Nguyen, J. De Beenhouwer, and J. Sijbers, *ImWIP: Open-source image warping toolbox with adjoints and derivatives*, SoftwareX, 24 (2023), p. 101524, https://www.sciencedirect.com/science/article/pii/S2352711023002200.

[20] J. Renders, J. Sijbers, and J. De Beenhouwer, *Adjoint image warping using multivariate splines with application to 4D-CT*, Medical Physics, 48 (2021), pp. 6362–6374.

[21] E. Y. Sidky and X. Pan, *Image reconstruction in circular cone-beam computed tomography by constrained total-variation minimization*, Phys. Med. Bio., 53 (2008), p. 4777–4807.

[22] T. Taillandier-Thomas, S. Roux, and F. m. c. Hild, *Soft route to 4D tomography*, Physical Review Letters, 117 (2016), p. 025501.

[23] W. van Aarle, W. J. Palenstijn, J. Cant, E. Janssens, F. Bleichrodt, A. Dabravolski, J. De Beenhouwer, K. J. Batenburg, and J. Sijbers, *Fast and flexible X-ray tomography using the ASTRA toolbox*, Optics Express, 24 (2016), pp. 25129–25147.

[24] G. Van Eyndhoven, K. J. Batenburg, and J. Sijbers, *Region-based iterative reconstruction of structurally changing objects in CT*, IEEE Transactions on Image Processing, 23 (2014), pp. 909–919.

[25] G. Van Eyndhoven, J. Sijbers, and J. Batenburg, *Combined motion estimation and reconstruction in tomography*, in Proceeding of the European Conference on Computer Vision (ECCV), 2012, pp. 12–21.

[26] V. Van Nieuwenhove, J. De Beenhouwer, T. De Schryver, L. Van Hoorebeke, and J. Sijbers, *Data-driven affine deformation estimation and correction in cone beam computed tomography*, IEEE Transactions on Image Processing, 26 (2017), pp. 1441–1451.

[27] H. Wu, A. Maier, R. Fahrig, and J. Hornegger, *Spatial-temporal total variation regularization (STTVR) for 4D-CT reconstruction*, in Proc. SPIE 8313, Medical Imaging 2012: Physics of Medical Imaging, 83133J, 2012.

[28] G. Zang, R. Idoughi, R. Tao, G. Lubineau, P. Wonka, and W. Heidrich, *Warp-and-project tomography for rapidly deforming objects*, ACM Transactions on Graphics, 38 (2019), pp. 1–13.

[29] M. Zehni, L. Donati, E. Soubies, Z. Zhao, and M. Unser, *Joint angular refinement and reconstruction for single-particle Cryo-EM*, IEEE Transactions on Image Processing, 29 (2020), pp. 6151–6163, https://github.com/Biomedical-Imaging-Group/CryoEM-Joint-Refinement.